International Journal of Solids and Structures 50(1), 97-110, 2013. Accepted for publication, Sept 13 2012.
See online version at http://dx.doi.org/10.1016/j.ijsolstr.2012.09.003

Plastic Deformation due to Reflected Detonation

James Karnesky[a], Jason Damazo[b,*], Kliulai Chow-Yee[c], Alexis Rusinek[d], Joseph E. Shepherd[b]

[a]*Air Force Research Laboratory WPAFB, OH 45431, USA*
[b]*California Institute of Technology, Pasadena, CA 91125, USA*
[c]*UC Berkeley, Berkeley, CA 94720, USA*
[d]*Laboratory of Mechanic, Biomechanic, Polymers and Structures National Engineering School of Metz (ENIM) Ile du Saulcy, Metz cedex, 57045 France*

Abstract

The deformation of tubes due to internal detonations and reflected shock waves was studied. In this paper, we report the experimental conditions and results for a series of experiments involving detonation loading of steel tubes alongside computational comparisons performed using an analytic one-dimensional model and a finite element simulation. To achieve plastic deformation, thin-walled steel tubes were filled with a stoichiometric ethylene-oxygen mixture and detonated. The range of initial pressures covered the span from entirely elastic to fully plastic deformation modes. A unique mode of periodic radial deformation was discovered. A model for the pressure load on the tube wall was developed and tested against experimental measurements.

Building on the experimental results, we discuss theoretical and computational models describing these experiments. The simplest model considers the oscillation of a single degree of freedom of the tube's cross section. Using this simple model, we explain that the periodic deformation observed in the experiment is the result of interference between the reflected shock wave and the elastic oscillations set in motion by the incident detonation. To capture the effects of boundary conditions and wave propagation, we performed computations using a two-dimensional axisymmetric model of the tube wall. For the mild steel tubes this required material testing, and the resulting constitutive relation proved to be limited. As a result, fidelity with experiments was much greater in the case of the stainless steel tubes.

Keywords: Gaseous detonation, Constitutive laws, Explosions, Finite element, Plasticity, Strain-rate

1. Introduction

A detonation (Lee, 2008; Fickett and Davis, 1979) is a shock wave coupled with and supported by a reaction zone. When a combustible mixture in a pipe undergoes detonation, the detonation wave propagates from the point of ignition to the end of the pipe (Shepherd, 2009). When the detonation reaches the closed end of a pipe, a reflected shock wave is formed to bring the flow immediately behind the detonation to zero velocity (Shepherd et al., 1991). This shock wave has an initial pressure of approximately 2.4–2.5 times (Shepherd et al., 1991) the pressure of the incident detonation wave. The shock decays as it propagates into the unsteady flow field of the detonation products. These pressure waves excite vibrations of the tubes and the elastic response has been extensively studied (Beltman and Shepherd, 2002). Depending on the tube geometry and the pressure of the incident detonation, the transient pressure immediately following the detonation reflection may result in plastic deformation or rupture of the tube.

In order to investigate the plastic deformation case, a series of experiments was conducted in which detonations were propagated within thin-walled steel tubes and reflected from a nearly rigid, reflecting boundary at the closed end. The large pressures associated with the detonation and reflection resulted in plastic deformation of the tubes. The tubes were instrumented with strain gauges to record time-resolved strains, and a micrometer and thickness gauge were used to measure residual plastic strains. Stoichiometric ethylene-oxygen was used as the test mixture at initial pressures of 0.5, 2, and 3 bar. Plastic deformation was observed to occur in all but the 0.5 bar cases. Repeated 2 and 3 bar experiments were performed in the same tube specimens to investigate the plastic strain ratcheting.

Pressure measurements and a simple model of reflec-

*Direct correspondence to damazo@caltech.edu, 1-626-395-3147

tion were used to develop a semi-empirical idealized one-dimensional internal loading history. This model used computed values for the detonation pressure, the Taylor–Zel'dovich (TZ) expansion, and the peak pressure of the reflected shock wave. An exponential decay rate was fit to the end-wall pressure trace, and the model was closed with the assumption of zero gradient behind the reflected shock. This model for the internal pressure was used to represent the internal conditions for a single degree of freedom structural model as well as a 2-D axisymmetric finite element model. For simplicity, we decided to perform completely decoupled simulations rather than coupled fluid-structure simulations as described by Deiterding et al. (2006).

A series of computations was performed using various material and structural models to compute the material response of the tube in the experiments. These computations provided both qualitative and quantitative insights into the mechanical behavior and the constitutive modeling requirements needed for prediction of plastic deformations driven by detonation.

2. Description of Experiment

The primary motivation of this series of experiments was to obtain detailed plastic strain measurements on a tube subjected to a well-defined detonation reflected shock loading with known boundary conditions. The experimental setup is illustrated in Fig. 1. The entire assembly is mounted on a track and an inertial mass is bolted to the far-right fixture. Test specimens were steel tubes with an inner diameter of 127 mm, a wall thickness of 1.5 mm, and a length of 1.2 m. The tubes were rolled and welded from sheets of either 1010 mild steel or 304L stainless steel. These tubes were coupled with a thick-walled tube of the same internal diameter and length. This thick-walled tube contained a glow plug to initiate a flame and obstacles to promote flame acceleration and DDT (deflagration to detonation transition), it was instrumented with pressure transducers along the wall in order to ensure that a fully developed Chapman–Jouguet (CJ) detonation propagated into the specimen tube.

The driver and specimen tubes were sealed in the center by a flange with two internal gland seals. This flange mated with a face-seal onto the open end of the thick driver tube, and the thin specimen tubes slipped into the gland seals. In order to achieve the desired fixed boundary condition, a collet was designed to clamp down on the reflecting end of the specimen tube. The collet was cut by wire-EDM out of tool steel and hardened. At 10 cm in length, the collet was designed such that the end point of the collet, when tightened, matched the face of the reflecting surface of the aluminum plug located inside the tube. A ring with an internal taper forced the collet closed and was bolted to a plate using 8 9/16"-18 bolts with minimum preloads of 68 N–m, resulting in a clamping force of at least 65,000 N. The collet assembly was securely fastened to a 2700-kg steel mass to absorb the recoil of the reflecting detonation. The collet and driver tube were held together with chains to prevent the force of the detonation from pulling the test specimen and driver tubes apart.

The specimen tubes were instrumented with Vishay brand strain gauges connected in a quarter bridge configuration. The model number and placement of these strain gauges varied between specimen tubes, but in general the strain gauges were concentrated near the reflecting end where the maximum deformation was observed to occur. Strain gauges were oriented to either align with the tube axis and record longitudinal strain or to be orthogonal to the axis thereby measuring hoop strains. The specific strain being plotted is included in each relevant figure. All tubes experienced multiple detonations that produced plastic deformation and so strain gauges were checked between experiments. For some experimental conditions, the gauges in high strain locations would break. Times at which failure occurs are clearly seen on the strain plots by the data spiking or going to zero depending on the failure mode incurred. In these cases, the gauges would be replaced between experiments in situ thereby avoiding the removal of the specimen tube from the experimental setup which might introduce errors in tube orientation. In addition to 3 pressure gauges in the driver tube, there was also a pressure gauge located in the center of the aluminum plug at the reflecting end. The placement of strain and pressure gauges in each experiment is included on the left-hand axis of the relevant plots. An example of this can be seen in Fig. 2 (a); note that the initial vertical offset corresponds to the physical separation between the gauges as given on the left-hand axis while the right-hand axis displays the gauge measurement. Residual plastic strain was recorded with post shot diameter and thickness measurements taken using an outside micrometer and a Checkline TI-007 ultrasonic wall-thickness gauge respectively.

In each experiment, the tube assembly was filled with stoichiometric ethylene–oxygen to initial pressure of 0.5, 2, or 3 bar. Plastic deformation was observed for each case except those with initial pressures of 0.5 bar. Repeated experiments on the same specimen tubes were performed with initial pressures of 2 and 3 bar to investigate strain ratcheting. Several specimen tubes were

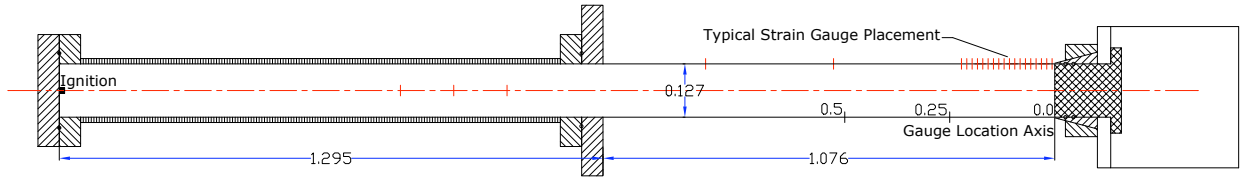

Figure 1: Detonation tube, dimensions in meters.

used in this series. All of the mild steel testing (tubes 4 and 7) was reported in Karnesky (2010) and portions of the stainless steel testing (tubes 9 and 11) was reported in Damazo et al. (2011). Here we will restrict discussion to tubes 4, 7, 9, and 11 which yielded the most pertinent results. The initial conditions for each of these tubes is included in Table 1.

Table 1: Summary of initial conditions used in experiments. In all cases, the mixture used was stoichiometric ethylene–oxygen.

	Material	P_0 (bar)	Test Numbers
Tube 4	1010 MS	0.500	1, 3, 5, 7, 9, 10
		2.000	2, 4, 6, 8, 11
Tube 7	1010 MS	0.500	1, 3, 5, 6, 7
		3.000	2, 4, 8
Tube 9	304L SS	0.500	1, 2, 4, 6, 8–10
		2.000	3, 5, 7, 11
Tube 11	304L SS	0.500	1, 3, 4
		3.000	2, 5

2.1. Results From Tube 4

The goal of the experiments performed in this tube was to investigate the strain ratcheting resulting from detonations of initial pressure 2 bar. Tube 4 was tested with 11 detonations, 5 shots resulted in plastic deformation with initial pressure 2 bar and 6 were elastic shots performed at initial pressure 0.5 bar to ensure that the gauges and data acquisition system were functioning properly.

The layout of the measurement locations is given in the figures where data is given. Figure 2 (a), for example, shows hoop strain measurements for strain gauges placed 25, 83, 140, and 197 mm from the location of detonation reflection. Figure 2 contains representative hoop and longitudinal strain traces from the five tests at 2 bar initial pressure. Examining Figs. 2 (a) and (b) we see three definitive times that show changes in the strain behavior. The first change in strain is a rise in longitudinal strain and a corresponding, but barely visible, dip

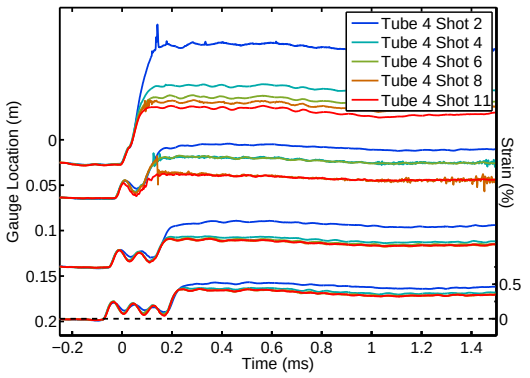

(a)

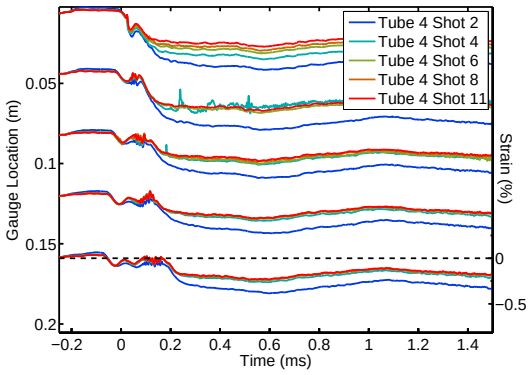

(b)

Figure 2: (a) Hoop and (b) longitudinal strain in mild steel tube 4 during five successive detonations of initial pressure 2 bar.

in hoop strain (indicating a decrease in tube diameter). These strains are the result of the longitudinal wave that is excited by the detonation and travels at the bar speed of the tube. Approximately 0.1 ms after the small dip is observed, the hoop strain undergoes a sudden increase and begins to oscillate at the natural frequency of the cross-section. This strain increase results from the flexural waves that travel with the detonation (Beltman and Shepherd, 2002). As shown in Fig. 2, the detonation travels from the gauge at 197 mm towards the gauge at 25 mm. When the detonation reaches the end-wall,

a reflected shock wave is created and propagates back into the tube from the gauge at 25 mm to the gauge at 197 mm. The peak pressure (and hence the strain) is highest for times soon after the detonation reflects.

The repeated tests show a substantial effect of strain hardening. The plastic strain increment on the first shot of a test series is always higher than that of the second and subsequent shots. This is particularly pronounced near the reflecting surface (gauge at 25 mm). One interesting feature of the deformation resulting from repeated shots was the formation of periodic ripples in the tube, shown in Fig. 3. The ripples had a mean peak-to-peak spacing of 63.0 mm. The distance between successive peaks was monotonically increasing away from the reflected end, with incremental gains per cycle averaging 1.3 mm. The computational work described in Section 5 explains this rippling behavior. The residual plastic strain taken after each experiment that resulted in plastic strain is plotted in Fig. 18 (a) alongside computational predictions as discussed in Section 6 quantifying the deformation attributed to this periodic deformation mode and shows that it is predicted by finite element analysis.

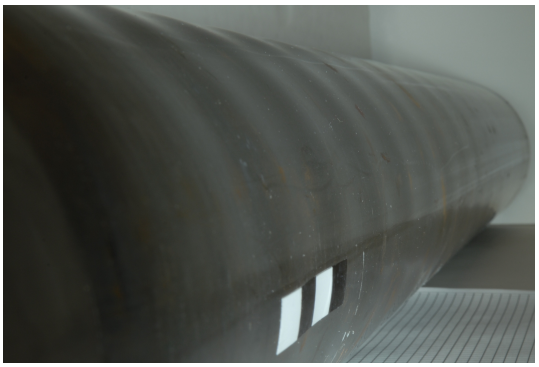

Figure 3: Rippling in mild steel tube 4 after five successive detonations of initial pressure 2 bar.

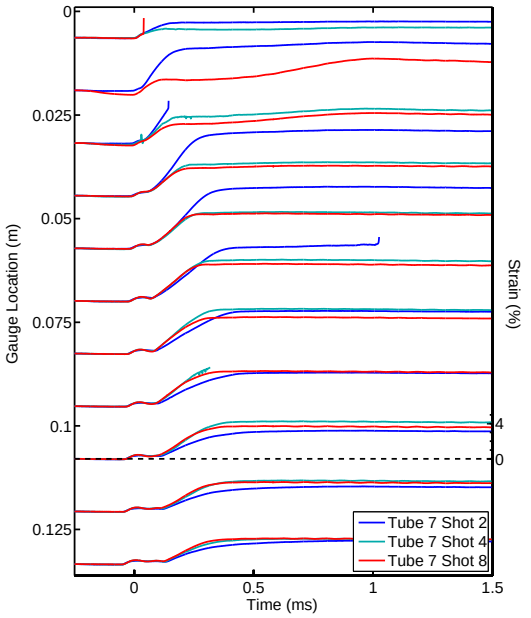

Figure 4: Hoop strain in mild steel tube 7 during three successive detonations of initial pressure 3 bar. Times at which data spikes or ceases represent gauge failure.

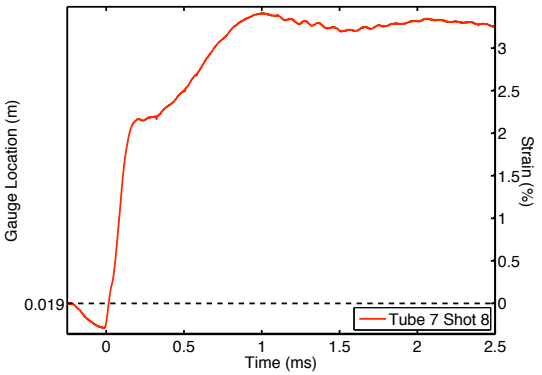

Figure 5: Hoop strain measured 19 mm from the reflecting end in mild steel tube 7 during the third detonation of initial pressure 3 bar.

2.2. *Results From Tube 7*

The experiments performed in this tube investigated strain ratcheting resulting from detonations of initial pressure 3 bar. A total of 8 experiments were performed in tube 7; three at 3 bar initial pressure and 5 elastic experiments at 50 kPa to test the apparatus. Initially, these tests showed the same hardening behavior as the 2 bar series. However, after a large reduction in strain increment due to hardening between the first two shots, the third shot showed a reduced effect of hardening. This is shown in Fig. 4. The third plastic shot in the tube also demonstrated a very interesting behavior in the vicinity of the reflecting boundary, as shown in Fig. 5. The first thing to notice is that the precursor is an order of magnitude larger than in the previous tests, peaking at 0.5% strain—well into the plastic regime. After this, the initial deformation of the tube due to the detonation and reflected shock wave follow the familiar pattern, occuring over 0.1 ms. Then, over the first millisecond following reflection, the strain continues to rise at a slower rate to a peak strain of three times that caused by the impulse of the reflected shock. A long-period vibration then sets in that is localized to the tube's reflecting end.

The cause of these behaviors remains unclear. However, one thing that is known is that the tube has undergone a large amount of plastic deformation and the strain gauge at 19 mm is at the elbow shown in Fig. 18 where the slope of the tube wall is drastic. Although the exact mechanism is unknown, it seems reasonable that this region of large variation in tube diameter and wall thickness would influence the longitudinal waves and perhaps cause the unexpectedly high strains before the detonation arrives.

It is also noteworthy that the frequency of the long-period vibration is on the same order as the breathing mode of the entire tube as predicted by commercial finite element software (SolidWorks, 2007) using a cylindrical shell with fixed boundaries. A discrete Fourier transform from the data for the 3 bar plastic deformation experiments was not useful as the slower frequencies ($f < 10$ kHz) were blurred over a range of 0 to approximately 4000 Hz due to the complexity of the signals. However, this mode is clearly seen in a discrete Fourier transform of the elastic strain data where the experiment reveals peaks at 13120 and 1556 Hz. The higher frequency oscillation is that of the single degree of freedom hoop oscillation mode (the rapid oscillation visible in Figs. 2 (a) and 4) and the slower oscillation corresponds closely to the breathing mode of the entire tube with an oscillation frequency of 1520 Hz. Studying the thickness measurements of the tube shown in Fig. 6 reveals that although the thickness measurement after the first 3 bar test showed largely the same qualitative behavior as the measurements made in tube 4, the measurements taken after the second 3 bar test are very different. There is a 38 mm wide region of near-constant thickness which shows a sharp decrease in thickness from the surrounding material, unseen in previous tests. This indicates that necking occurred in the material during the test. Therefore we speculate that in the 2 bar tests and earlier 3 bar tests the force associated with the mode shown in Fig. 5 was absorbed by the boundary, but the combination of the necking and the rapid change in the tube outer diameter meant that, in the later 3 bar tests, this force was instead supported by the tube wall and resulted in the observed long-time oscillating strain behavior. I.e., it appears that this region is acting as a plastic hinge responding to the breathing mode. This also explains why the peak outer diameter increased between the two tests; strain hardening would tend to decrease this change (as was observed for the 2 bar tests), but the plastic instability causes large strains.

Unlike tube 4, detonations in tube 7 did not produce a rippled surface in tube. This is seen in the residual plastic strain measurements given in Fig. 18 (b). Because the point of plastic instability was approached in these tests, and the experimental facility was not set up to contain blast waves resulting from tube rupture, no further plastic experiments were performed in tube 7.

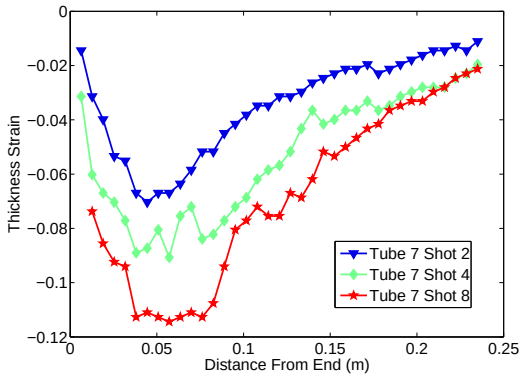

Figure 6: Residual plastic thickness strain of mild steel tube 7 after each of three successive detonations of initial pressure 3 bar.

2.3. *Results From Tube 9*

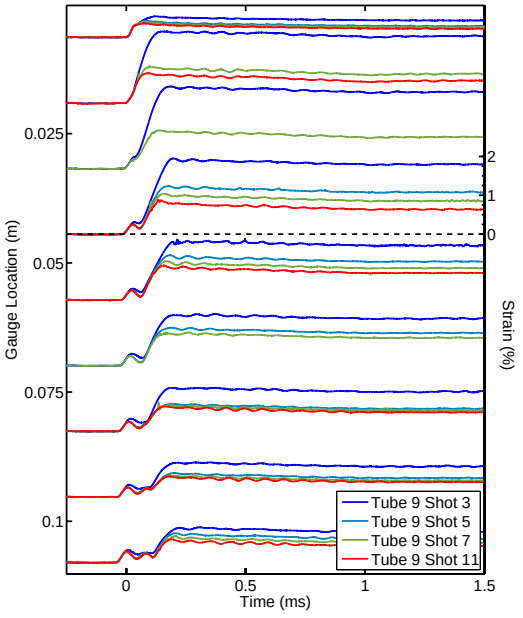

Figure 7: Hoop strain in stainless steel tube 9 during four successive detonations of initial pressure 2 bar.

It was the objective of the detonation experiments performed in tube 9 to repeat the experiments performed in tube 4, but with tubes constructed of 304L stainless steel so that more accurate numerical comparisons may be obtained by using a better characterized material.

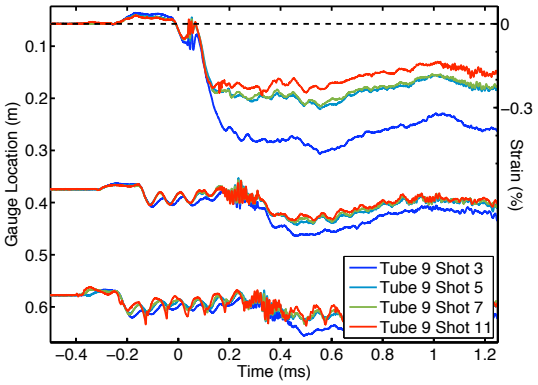

Figure 8: Longitudinal strain in stainless steel tube 9 during four successive detonations of initial pressure 2 bar.

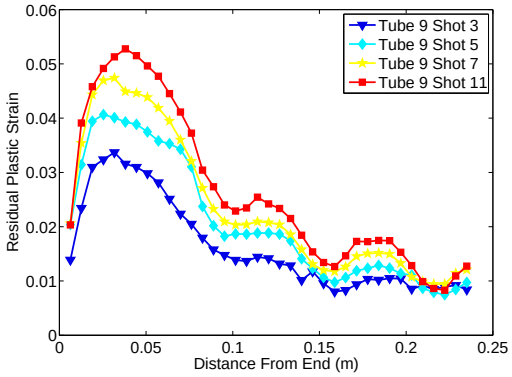

Figure 9: Residual plastic hoop strain of stainless steel tube 9 after each of four successive detonations of initial pressure 2 bar.

Figures 7 and 8 depict hoop and longitudinal strain data respectively for each of the five experiments in tube 9 that resulted in plastic deformation. Comparing the stainless steel results shown in Figs. 7 and 8 to the mild steel results given in Fig. 2 reveals similar strain profiles in the mild steel and stainless steel tubes. The primary observed difference is that the stainless steel tube undergoes larger strains for identical internal pressures due to a lower yield stress in stainless steel compared to mild steel. Residual plastic strain measurements as plotted in Fig. 19 reveal that the rippled tube surface is again visible in tube 9.

Figure 9 displays the residual plastic strain in tube 9 after the five plastic deformation detonation experiments. The ripple pattern that was seen clearly in mild steel tube 4 is again seen in in stainless steel tube 9. Figure 9 shows residual plastic strain measurements taken after each subsequent plastic deformation experiment and reveals the mean ripple wave length to be 70 mm.

2.4. *Results From Tube 11*

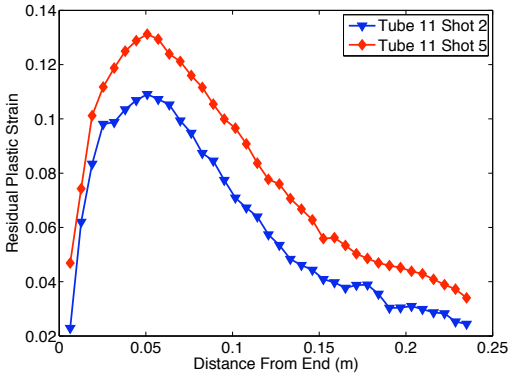

(a)

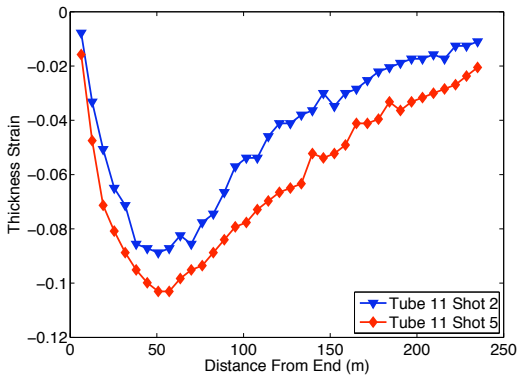

(b)

Figure 10: Residual plastic (a) hoop and (b) thickness strain for stainless steel tube 11 after two successive detonations of initial pressure 3 bar.

Tube 11 repeated the 3 bar initial pressure detonation experiments performed in tube 7 with the different tube material of 304L stainless steel. Strain gauge failure caused by the increased deformation of the stainless steel tubes meant that no time-resolved strain results are reported for this tube. Residual plastic hoop and thickness train were recorded as usual. Figure 10 reports the residual plastic hoop and thickness strain data. Similar qualitative trends are observed as seen in mild steel tube 7. The primary differences between the tubes are the increased strain levels in tube 11 due to the decrease in material strength and the absence of observable necking in the thickness strain data. Even though the plastic instability was not observed, only two detonation experiments of initial pressure 3 bar were performed in the stainless steel tube so as to avoid catastrophic tube rupture. The residual plastic strain data for all experiments will be the primary point of comparison as we move to the computational results.

3. Pressure Loading Model

The reflection of a detonation wave from the closed end of a tube produces an unsteady flow field and a decaying shock wave. In order to numerically compute the structural response of the tube arising from a detonation and its reflection, it is necessary to specify the pressure history everywhere along the tube interior. Although this can be done with computational fluid dynamics, we have developed a simple alternative in the form of a semi-empirical model based on analysis and experimental observations.

3.1. Model Description

Detonation waves propagating inside of a closed tube create a pressure wave that travels from the point of ignition toward the closed end of the tube. The gas immediately behind the detonation wave is moving but is slowed down to zero velocity by the expansion wave following the detonation. This expansion wave is known as the Taylor or Taylor-Zel'dovich (1950; 1940) wave for their derivations of the flow field. The spatial and temporal distribution of pressure for the entire tube prior to the arrival of the reflected shock wave may be solved for explicitly from the method of characteristics (Zel'dovich and Kompaneets, 1960; Shepherd et al., 1991; Fickett and Davis, 1979). The resulting pressure, sound speed, and fluid velocity distributions are

$$P(x,t) = \begin{cases} P_1 & U_{CJ} < \frac{x}{t} < \infty \\ P_3\left[1 - \frac{\gamma-1}{\gamma+1}\left(1 - \frac{x}{c_3 t}\right)\right]^{\frac{2\gamma}{\gamma-1}} & c_3 < \frac{x}{t} < U_{CJ} \\ P_3 & 0 < \frac{x}{t} < c_3 \end{cases} \tag{1}$$

$$c(x,t) = \begin{cases} c_1 & U_{CJ} < \frac{x}{t} < \infty \\ c_3\left[1 - \frac{\gamma-1}{\gamma+1}\left(1 - \frac{x}{c_3 t}\right)\right] & c_3 < \frac{x}{t} < U_{CJ} \\ c_3 & 0 < \frac{x}{t} < c_3 \end{cases} \tag{2}$$

$$u(x,t) = \begin{cases} 0 & U_{CJ} < \frac{x}{t} < \infty \\ \frac{2c_3}{\gamma+1}\left(\frac{x}{c_3 t} - 1\right) & c_3 < \frac{x}{t} < U_{CJ} \\ 0 & 0 < \frac{x}{t} < c_3 \end{cases} \tag{3}$$

where γ is the effective ratio of specific heats in the products computed on the basis of chemical equilibrium (see Wintenberger et al., 2004; Radulescu and Hanson, 2005). The subscript 1 denotes the pre-detonation region, and the subscript 3 denotes the post-expansion region. The Taylor wave parameters may be found from the CJ state to be

$$\begin{aligned} c_3 &= \frac{\gamma+1}{2} c_{CJ} - \frac{\gamma-1}{2} U_{CJ}\,, \\ P_3 &= P_{CJ}\left(\frac{c_3}{c_{CJ}}\right)^{\frac{2\gamma}{\gamma-1}} \end{aligned} \tag{4}$$

where c_{CJ} is the sound speed at the CJ state.

When the detonation wave reaches the end wall, a reflected shock wave is created in order to bring the moving gas immediately behind the detonation wave back to rest. In experiments, this is observed on the pressure transducers as a second pressure pulse following the incident detonation. In order to fully model the pressure, it is necessary to carry out a computational fluid dynamics simulation of the gas dynamics in the tube. However, if we are only interested in the first reflected wave, then it is possible to make some simplifying assumptions and create a semi-empirical model for the amplitude of the reflected wave. At the instant of reflection, the shock wave has a peak pressure of about $2.4-2.5 P_{CJ}$ and travels at a much lower speed than the incident detonation. The reflected shock decays in both speed and peak pressure as it moves away from the end wall. Numerical simulations of the flow (Shepherd et al., 1991; Ziegler, 2010) predict that there is a very small pressure gradient between the reflected wave and the end wall until the tail of the expansion wave is reached. One such simulation is shown in Fig. 11. These calculations were done with

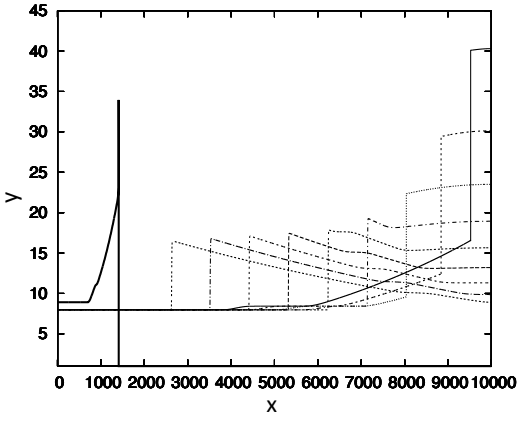

Figure 11: Spatial pressure profiles from reacting Euler calculations of a reflecting detonation. x-axis is half-reaction zone widths, y-axis is normalized pressure (Ziegler, 2010).

the reacting Euler equations and one-step chemistry and a second order accurate min-mod slope-limited MUSCL scheme (Deiterding, 2003). The conditions were a detonation with nodimensional heat release of 50, γ of 1.2, overdrive 1.01, and a reduced activation energy of 3.71.

The initial condition included the TZ expansion, and the domain is 10,000 half reaction zone widths with a base grid of 4000 cells and 3 levels of refinement with factors of 2, 4, and 4 (Ziegler, 2010). There is a minimal gradient immediately after reflection, when the pressure is highest. As the reflected shock propagates back up the tube and out of the TZ expansion, there is an inflection in this gradient, and it develops into a triangular pulse shape at later times. By this time, however, the post-shock pressure has decayed to below the CJ pressure of the incident detonation. Based on this observation, we have made the approximation that there is zero pressure gradient behind the reflected shock, so that the pressure just behind the shock is equal to the pressure at the end wall at each point in time. This approximation is only valid for sufficiently short times following reflection. In the case of long times, an expansion wave will develop behind the reflected shock and the pressure gradient cannot be neglected.

Assuming that the pressure P_R behind the reflected shock is known, we can use the shock jump relations to find the velocity U_R of the reflected shock. The result is

$$U_R(t) = -u(x,t) + c(x,t)\sqrt{\frac{\gamma+1}{2\gamma}\left[\frac{P_R(t)}{P(x,t)} - 1\right] + 1}\ , \tag{5}$$

where $u(x,t)$ and $P(x,t)$ are the velocity and pressure just upstream (to left) of the reflected shock, as determined by the Taylor wave solution given previously. The trajectory $X_R(t)$ of the reflected shock can be determined by integration as

$$\frac{dX_R}{dt} = -U_R(t) \qquad \text{where} \qquad X_R(t = t_0) = L\ . \tag{6}$$

where $t_o = L/U_{CJ}$ is the time of wave reflection.

To use our method of computation, the pressure-time history of the shock must be known from either experimental measurement or simulation. Using the zero-pressure gradient assumption discussed above, the present results approximate the reflected shock pressure as the measured pressure history at the end wall $x = L$. The measured pressure history at the end wall for a typical test is shown as the gauge located at 0 m in Fig. 12. Since this is quite noisy and the tabulated data is inconvenient for numerical simulation, we have fit the pressure history to a simple exponential decay form as used in previous studies (Beltman and Shepherd, 2002) on elastic vibrations of tubes:

$$P_R(t) = \left(P_{CJref} - P_3\right)\exp\left[-(t - t_o)/\tau\right] + P_3\ . \tag{7}$$

In order to limit the number of parameters that must be obtained from experimental data, we have set the peak pressure P_{CJref} and the final pressure P_3 to be those computed for the ideal reflection of a CJ detonation wave using realistic thermochemistry (Browne et al., 2008). The decay time τ is found by fitting the measured pressure trace to equation (7).The parameters used for our experiment are shown in Table 2. Combining this solution for the reflected wave with the previous analytical solution for the Taylor wave, the pressure $P(x,t)$ within the tube following detonation reflection is now completely specified.

Table 2: Parameters used in the pressure model for stoichiometric ethylene-oxygen mixtures.

$\mathbf{P}_1$ **bar**	$\mathbf{U}_{CJ}$ **m/s**	$\mathbf{P}_{CJ}$ **MPa**	$\mathbf{c}_{CJ}$ **m/s**	γ	$\mathbf{P}_{ref}$ **MPa**	τ μ**s**
0.5	2343	1.643	1264	1.138	4.120	330
2.0	2410	6.831	1303	1.143	17.15	300
3.0	2430	10.54	1316	1.146	26.46	296

3.2. Model Validation

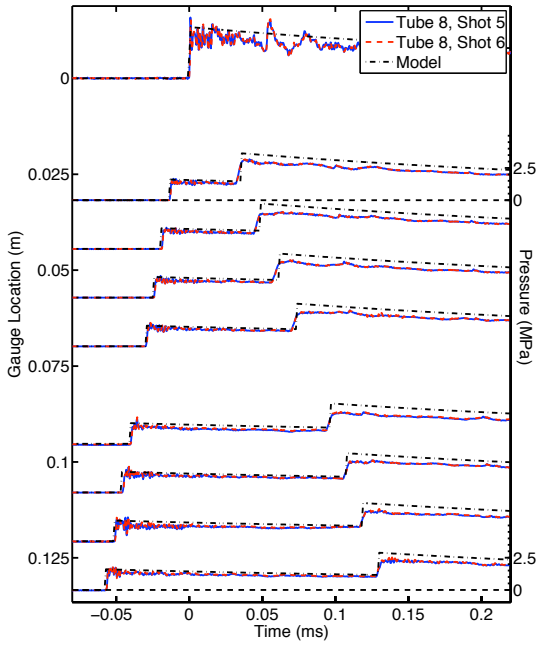

Figure 12: Pressure-time traces for all reflecting end gauges. Data from two subsequent detonations are shown to illustrate experiment repeatability.

The experimental setup described above was modified to include pressure gauges in the immediate vicinity of the reflecting end wall so that the pressure of the

reflected shock wave may be measured. This entailed cutting holes for the pressure gauges in the wall of the tube and fastening a mount to hold the pressure gauges in place. Since the aluminum mount would only seal to an undeformed tube and the holes cut in the tube wall produced stress concentrations, we could not plastically deform the tube nor would any measured strains be reliably close to the previous experiments. Hence no strain gauges were used in this series of experiments. Four pressure gauges were used in the thick driver tube and 9 pressure gauges were placed on or near the reflecting wall with gauge locations given on the plot. The gauge at 0 m was placed in the center of the reflecting wall. The other gauges were placed the printed distance from the reflecting end so that the gauge's surface was flush with the inner surface of the tube. Figure 12 has the resulting pressure traces spaced proportional to the actual gauge locations.

There are two measures of fidelity that determine the accuracy of this model. The first is the speed of the reflected shock wave and the second is the pressure profile. Figure 12 shows that the model predicts the arrival time accurately; the mean error in arrival time for these gauges was 2.3 μs. The model is less accurate in predicting the peak pressure—the model tends to over-predict peak pressures on the reflected shock by up to 20%.

The pressure gauges nearest the reflecting end also reveal a behavior that is not captured by our model. When the reflected wave arrives, the model predicts a sharp increase in pressure; however, the data show a more gradual rise. This is especially evident in gauges at 44 and 32 mm. This is most likely due to reflected shock wave bifurcation resulting from shock wave boundary layer interaction. Near the tube wall there is a boundary layer that transitions the flow from the velocity behind the detonation wave to zero velocity at the tube wall. As the shock wave reflects into this boundary layer a compression wave, or series of shocks, results rather than a single shock.

Despite the discrepancies in the amplitude of the pressure peaks for the reflected wave, the data seen in Fig. 12 illustrate the usefulness of this model in predicting the speed and strength of the incident detonation and reflected shock wave. We used this model of the pressure loading in the single degree of freedom and finite element calculations described in Sections 5 and 6.

4. Material Modeling

Material models were explored so that the deformation may be properly computed for both the tubes composed of 1010 mild steel (tubes 4 and 7) and 304L stainless steel (tubes 9 and 11). The strains observed in the experiments were strictly less than the failure strains for mild and stainless steel, thus no failure criterion was implemented in the numerical models. The simplest model employed was an elasto-plastic model with linear strain hardening; this model was used with the single degree of freedom calculations discussed in Section 5. In such a system the stress may be related to the strain by the equation

$$\sigma = E_1 \epsilon \quad \text{for} \quad \epsilon < \epsilon_y \tag{8}$$

$$\sigma = \sigma_y + E_2(\epsilon - \epsilon_y) \quad \text{for} \quad \epsilon > \epsilon_y \, . \tag{9}$$

In order to apply this material model with hardening, the yield strain must be monitored as it increases in the plastic regime. This is done through the additional equation

$$\frac{d\sigma_y}{dt} = \frac{\partial \sigma_y}{\partial \sigma} \frac{\partial \sigma}{\partial \epsilon} \frac{\partial \epsilon}{\partial t} \tag{10}$$

where

$$\frac{d\sigma_y}{d\sigma} = \begin{cases} 1 & \sigma \geq \sigma_y \\ 0 & \sigma < \sigma_y \end{cases} \, . \tag{11}$$

The parameters used for the mild and stainless steel tubes are given in Table 3. This simple material model was adequate for the single degree of freedom computations because it was the goal of the single degree of freedom model to gain basic understanding into the deformation behavior. The detailed finite element analysis discussed in Section 6 required a more accurate material model.

Table 3: Material properties used in single degree of freedom calculations.

	Mild Steel	Stainless Steel
E_1 (GPa)	210	200
E_2 (GPa)	1	1
ρ (kg/m^3)	7800	7900
h (mm)	1.5	1.5
R (mm)	63.5	63.5
ν	0.3	0.3
ϵ_y (%)	0.3	0.3

Two material models were used in the finite element computations. The Johnson-Cook model (1983) was chosen as the preferred method to account for strain-rate hardening and was the only model used to describe the stainless steel tubes (tubes 9 and 11). The high-strain rate plastic deformation of the mild steel tubes (tubes 4 and 7) had not been previously characterized. This meant that the tube material had to be tested in

order to arrive at a constitutive relation which could be input to a computational model of the tube. Samples of the tube were cut and subjected to testing in a double shear test at strain rates from 10^{-3} to 10^{2} s^{-1} as described in Rusinek and Klepaczko (2000) and the results were presented in Sauvelet et al. (2007) with the data points given in Fig. 13. Various attempts to fit the Johnson-Cook parameters (both full and simplified) to the measured stress–strain–strain-rate data for the mild steel were unsuccessful in generating a material model yielding reasonable results for the mild steel. Instead, strain-rate hardening was incorporated via the Cowper-Symonds (1957) model using a trilinear strain-hardening curve where σ may be calculated from

$$\sigma = \begin{cases} E_1\epsilon & \epsilon \le \epsilon_{y,1} \\ E_2\epsilon + \Delta E_{12}\epsilon_{y,1} & \epsilon_{y,1} < \epsilon \le \epsilon_{y,2} \\ E_3\epsilon + \Delta E_{23}\epsilon_{y,2} + \Delta E_{12}\epsilon_{y,1} & \epsilon_{y,2} < \epsilon \end{cases} \tag{12}$$

where $\Delta E_{ij} = E_i - E_j$. The Cowper-Symonds model specifies strain rate sensitivity by defining the first yield point ($\epsilon_{y,1}$) to be a function of the strain rate as given in Eq. (13). The parameters and yield strain at zero strain-rate were fit to the data of Sauvelet et al. (2007) using least squares error minimization, and the values used in the final computations are included in Table 4. The results of the fit are shown in Fig. 13.

$$\sigma_{y,1} = \epsilon_{y,1}E_1 = \sigma_{y,0}\left[1 + \left(\frac{\dot{\epsilon}}{C}\right)^{1/P}\right] \tag{13}$$

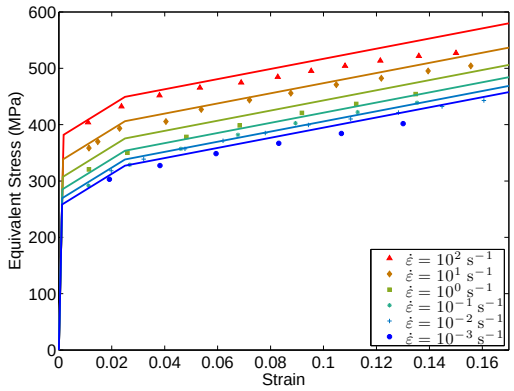

Figure 13: Cowper-Symonds rate-hardening model used in mild steel computations. The lines are computed from Eq. (12) with properties given in Table 4; the model is compared with measured data from Sauvelet et al. (2007).

Unlike the mild steel, 304L stainless steel is well characterized by the Johnson-Cook material model for strains and strain rates in the range observed in the experiments presented here. In these experiments, the strain level is sufficiently low that the temperature increase does not induce a thermal softening of the material and the process of phase transformation for 304L stainless is not encountered (Zaera et al., 2012). Hence the flow stress is adequately defined by the temperature independent form of the Johnson-Cook model, shown in Eq. (14), which was used in all stainless steel finite element computations.

Table 4: Mild steel material properties used in the finite element simulations.

	Bilinear (2 bar)	Bilinear (3 bar)	Cowper-Symonds
E_1 (GPa)	210	210	210
E_2 (GPa)	1	1	3
E_3 (GPa)	N/A	N/A	1
$\epsilon_{y,0}$ (%)	0.125	0.28	0.1
$\epsilon_{y,2}$ (%)	N/A	N/A	2.5
C	N/A	N/A	2000
P	N/A	N/A	6.6

Table 5: Johnson-Cook material properties used in the finite element simulations for 304L SS tubes (Lee et al., 2006).

A (MPa)	310
B (MPa)	1000
n	0.65
c	0.07
$\dot{\epsilon}_{p,0}$ (s^{-1})	1.00
E_1 (GPa)	200

$$\sigma_y = \left(A + B\overline{\epsilon}_p^{\,n}\right)\left[1 + c\ln\frac{\dot{\overline{\epsilon}}_p}{\dot{\epsilon}_{p,0}}\right] \tag{14}$$

Where $\overline{\epsilon}_p$ is the von Mises equivalent plastic strain. The Johnson-Cook material parameters used in the finite element simulations are given in Table 5.

5. Single Degree of Freedom Model

The simplest theoretical model of the dynamics of a tube wall considers an infinite tube subjected to a spatially uniform, time-dependent loading. If the stresses in the tube wall are assumed to be uniform, and displacements are small compared to the tube radius R, then the equation of motion for such a system is

$$\rho h\frac{d^2x}{dt^2} + \frac{h}{R}\sigma = \Delta P(t)\ . \tag{15}$$

While in the elastic regime, the membrane stress in the tube wall is related to the strain by

$$\sigma = \frac{E_1}{1-\nu^2}\epsilon_\theta \,, \tag{16}$$

where the hoop strain ϵ_θ is

$$\epsilon_\theta = \ln\left(\frac{R+x}{R}\right) \approx \frac{x}{R} \text{ for } x \ll 1 \,. \tag{17}$$

The elastic equation of motion then becomes

$$\rho h \frac{d^2x}{dt^2} + \frac{E_1 h}{R^2\left(1-\nu^2\right)}x = \Delta P(t) \,. \tag{18}$$

This is the equation for a forced harmonic oscillator with natural frequency

$$\omega = \frac{1}{R}\sqrt{\frac{E_1}{\rho\left(1-\nu^2\right)}} \,. \tag{19}$$

The period of the hoop oscillation of the cross section is $T = 2\pi/\omega$, which for the material properties given in Table 3 is $T_{ms} = 73$ μs for mild steel tubes and $T_{ss} = 76$ μs for stainless steel tubes. This is also four times the characteristic response time for the cross section to a differential pressure loading.

The single degree of freedom model may also be extended to the plastic regime by introducing an inelastic stress-strain relationship into Eq. 15. This was done with the elasto-plastic model with linear strain hardening (Eqs. 8–11) introduced in Section 4. All results of the single degree of freedom model discussed herein are for mild steel, but qualitatively the same effects occur for stainless steel tubes.

This model has been implemented in Matlab using the Runge–Kutta solver `ode45` over a range of axial locations and pressure loadings and is plotted in Fig. 14. The pressure loading $P(t)$ for a given location is computed by the pressure model developed in Section 3 for stoichiometric ethylene–oxygen detonations of initial pressure 50, 200, and 300 kPa. Varying the axial location at which we compute the strain causes the reflected shock wave to arrive at different phases of the elastic oscillation. The axial location for each case plotted in Fig. 14 is chosen such that the reflected shock wave arrives half-way between the third peak and the third trough of the oscillation. This corresponds to locations 155, 161, and 169 mm from the end wall for the 50, 200, and 300 kPa initial pressure cases respectively.

These three initial pressures correspond to three distinct response regimes. The first regime is when the deformation is entirely elastic through both incident and reflected waves as shown in Fig. 14a; this case corresponds to a stoichiometric ethylene–oxygen detonation of initial pressure 50 kPa. The behavior observed in Fig. 14a is the arrival of the incident detonation wave at A as observed by the increase in stress and strain and the onset of hoop oscillations with a frequency given by Eq. (19). The peak stress and strain induced by the incident wave occurs during the first oscillation peak at B. The pressure behind the detonation front decreases through the Taylor wave and thus we observe the stress and strain local maxima of each oscillation correspondingly decrease. The reflected shock wave arrives at C. The large pressures resulting from reflection results in the overall maximum stress and strain at D. Without damping, the stress and strain oscillations continue indefinitely centered at a value corresponding to the final burned gas pressure.

Increasing the initial pressure to 200 kPa results in the second stress–strain regime wherein the strains are entirely elastic through the incident detonation and only become plastic upon the arrival of the reflected shock wave as shown in Fig. 14b. Despite the onset of plasticity, many of the same features seen in the purely elastic case are still observed. The detonation arrives at A, the stress and strain peak during the first oscillation at B. The reflected shock wave, which arrives at C, causes the material to yield plastically as visualized in the stress–strain inset. The stress and strain peak at D and then begin elastic oscillation as the material is unloaded. Examining Eq. (15) we note that for the 200 kPa initial pressure case, the magnitudes of the stress term at B (corresponding to the maximum elastic oscillation before the arrival of the reflected shock wave) and the pressure behind the reflected shock wave are of the same order:

$$\left.\frac{h}{R}\sigma_B\right|_{2\text{ bar}} = 16.6 \text{ MPa} \tag{20}$$

$$\left.\Delta P_{CJ,ref}\right|_{2\text{ bar}} = 17.1 \text{ MPa} \tag{21}$$

suggesting that the elastic oscillation may significantly affect the total residual plastic strain. This effect is plotted in Fig. 15a and b by computing the deformations at locations 177 and 144 mm respectively; these locations correspond to the reflected shock wave arriving at a local minimum and a local maximum in the elastic oscillation. At first glance it would seem that the deformation would be larger in case b when the reflected wave arrives at a stress peak—the stress begins at a higher value and this point is closer to the end wall implying that the internal pressure is greater. However, Fig. 15 reveals that the opposite is in fact true. Larger strains occur for the point 177 mm from the end wall where the

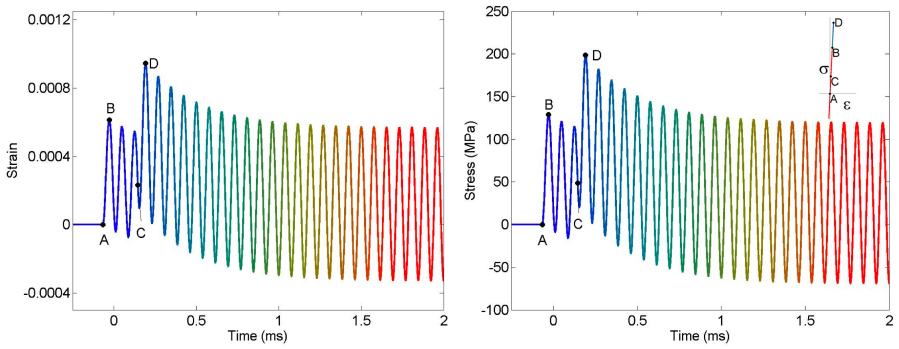

(a)

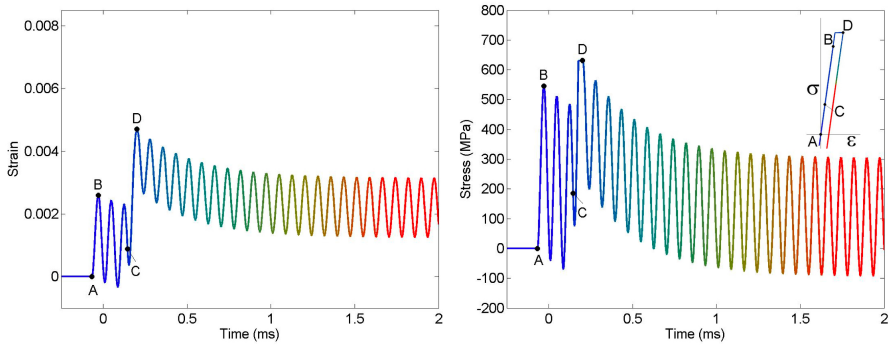

(b)

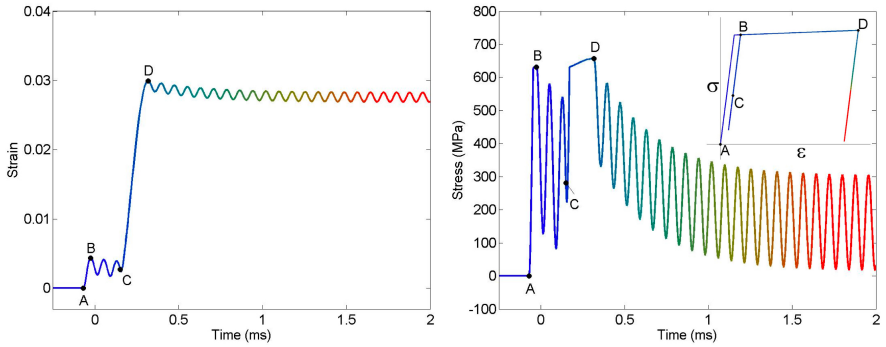

(c)

Figure 14: Hoop stress–hoop strain curves showing mild steel material response as determined by the single degree of freedom model to stoichiometric ethylene–oxygen detonation of initial pressure (a) 50 kPa, (b) 200 kPa, and (c) 300 kPa. In each case the detonation arrives at *A* and the reflected shock wave at *C*. *B* marks the maximum stress/strain achieved before the reflected shock arrives and *D* marks the overall stress/strain maximum.

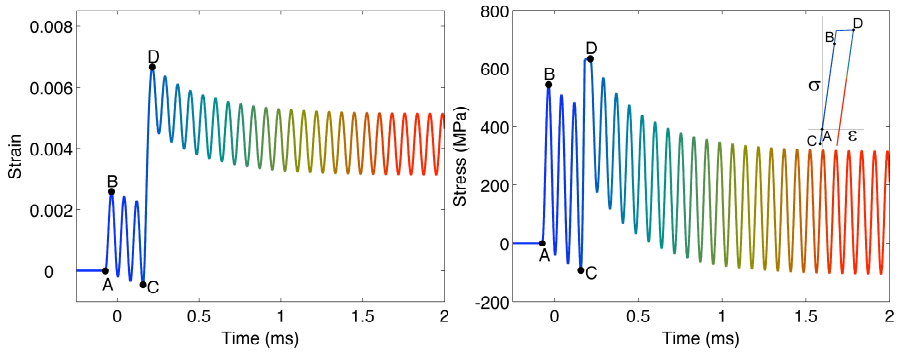

(a)

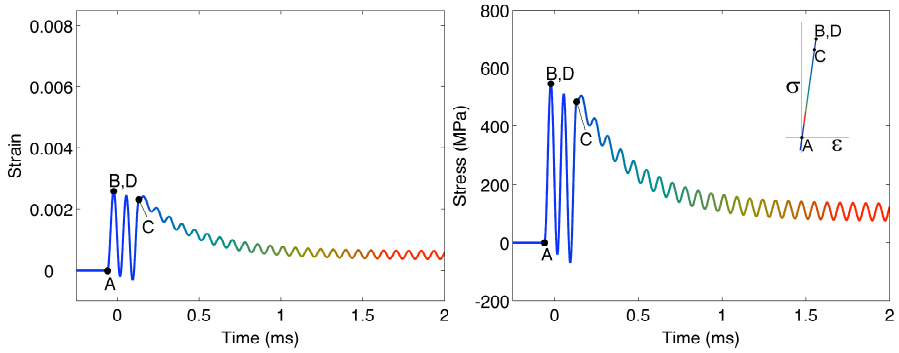

(b)

Figure 15: Hoop stress–hoop strain curves showing mild steel material response as determined by the single degree of freedom model to detonation of initial pressure 200 kPa. In (a) the reflected shock wave arrives at a stress/strain minimum while in (b) the reflected shock arrives at a stress/strain maximum. *A* marks the arrival of the incident detonation and *C* marks the arrival of the reflected shock. The maximum stress/strain achieved before the arrival of the reflected shock wave is denoted by *B* and the overall stress/strain maximum is at point *D*.

pressure is lower and the reflected wave arrives in a local stress/strain minimum. This is explained by solving Eq. (15) for d^2x/dt^2:

$$\frac{d^2x}{dt^2} = \frac{\Delta P(t)}{\rho h} - \frac{\sigma}{\rho R} \,. \tag{22}$$

The pressure differential is always positive and thus constructive interference occurs when the reflected wave arrives while the stress is negative. Therefore the largest accelerations are produced when the reflected wave arrives during a stress minimum as seen in Fig. 15a. When the reflected shock arrives during a stress maximum as in Fig. 15b, Eq. (22) indicates that destructive interference occurs. Hence the phase of the elastic oscillation when the reflected shock wave arrives substantially affects the residual plastic strain. In the particular case shown in Fig. 15b, the pressure and stress terms are closely matched in magnitude and sign which results in the elastic oscillation being nearly extinguished by the arrival of the high-pressure reflected wave. In this case, the strains remain entirely elastic and never reach the maximum achieved by the incident detonation wave even though the pressure is larger behind the reflected shock wave. This effect is also observed in the 50 kPa initial pressure case, but even with the interference the strains never reach plasticity.

The third and final stress–strain regime is given in Fig. 14c where the deformation is plastic for both incident and reflected waves. This corresponds to a detonation of initial pressure 300 kPa. Here we see the detonation arrive at *A*, cause the material to yield to a maximum at *B*, and then begin elastic oscillation as the material unloads. This unloading is interrupted by the arrival of the reflected wave at *C* which results in the majority of the plastic deformation. Unlike the 50 and 200 kPa initial pressure cases, the large strains of the 300 kPa initial pressure case implies that the elastic oscillation is a relatively small feature of the deformation and that the resulting strain is dominated by the plastic deformation of the reflected wave. In this case, the

reflected pressure is large enough such that the forcing term of Eq. (15) is substantially greater than the stress term and thus, even though the same interference observed in the 200 kPa initial pressure case occurs, its effect represents only a small portion of the total computed strains.

Examining the plastic strains over an array of spatial locations for the 200 kPa initial pressure case further elucidates the effect of the stress–pressure interference. The residual plastic strains are plotted in Fig. 16. The most striking thing about these results is the presence of the ripples that were noted in the experiment. The rippling is present in one-dimensional single degree of freedom calculations, which are free of any effect of boundary conditions or bending stresses, demonstrating that the primary cause of the phenomenon is the interference of the pressure and stress terms of Eq. (15). In other words, the incident detonation sets the wall of the tube in elastic vibration at the natural frequency of the cross section. The subsequent arrival of the reflected shock then imposes a second impulsive pressure loading on the already vibrating wall. Depending on the phase of the oscillation at the time when the shock wave arrives, the reflected shock loading may either augment or diminish the tube deformation. In the range of deformation produced by the tests at 2 bar initial pressure, the stress and pressure terms are of similar magnitudes resulting in either constructive interference and correspondingly large plastic strain or destructive interference wherein the material motion is stilled and no permanent deformation ensues. This produces the periodic ripples observed in the data and explains why the ripples are most pronounced in the 200 kPa initial pressure experiment.

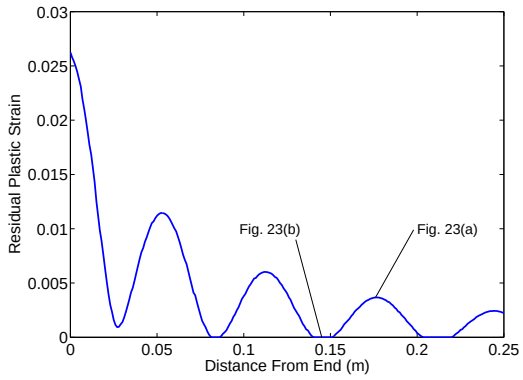

Figure 16: Single degree of freedom model results for residual plastic hoop strain in a mild steel tube after the first 2 bar initial pressure detonation loading cycle. The marked points are the locations plotted in Fig. 15.

Knowing the mechanism behind the formation of the ripple pattern allows the calculation of the ripple wavelength. This is dependent on the reflected shock velocity, which increases in the TZ wave and decreases beyond the expansion tail, so we will analyze this in terms of the average shock velocity $\overline{U}_R$ which is a function of axial distance from the point of detonation reflection. The total time between the arrival of the detonation wave and the reflected shock at a given location x_0 is

$$\Delta t = \frac{x_0}{U_{CJ}} + \frac{x_0}{\overline{U}_R} = \frac{\overline{U}_R + U_{CJ}}{\overline{U}_R U_{CJ}} \cdot x_0 \tag{23}$$

and the total time difference required for the reflected wave to arrive at locations 360° out of phase of the elastic oscillations at a given point is

$$\Delta t_2 - \Delta t_1 = \frac{1}{f_{xs}} \tag{24}$$

where $f_{xs} = \omega/2\pi$ is the natural frequency of the cross section. The wavelength of the ripples, λ_r is then estimated to be

$$\lambda_r = x_2 - x_1 = \frac{1}{f_{xs}} \left(\frac{\overline{U}_R U_{CJ}}{\overline{U}_R + U_{CJ}} \right). \tag{25}$$

Evaluating this expression with the numbers for the 2 bar condition used in the experiment, $U_{CJ} = 2400$ m/s, $f = 12.8$ kHz, and the average velocity of the reflected shock computed from its arrival time at the second peak in the ripples, $\overline{U}_R = 1380$ m/s, the resulting wavelength is 68.6 mm. The peak-to-peak spacing for this location in the experiment was 70 mm, within 2% of our estimate.

6. Finite Element Analysis

A more sophisticated computational investigation of the problem involves the use of the method of finite elements. For the results reported herein, the finite element solver LS-DYNA V970 (2005) was used. Figure 17 shows the typical numerical mesh for the tube. The tube was modeled using two-dimensional axisymmetric shell elements with selective-reduced integration over a 2 by 2 Gaussian quadrature. Typically 6 nodes were used through the thickness and 4000 through the tube length, which was taken to be 2 m. This was in an effort to mimic the overall length of the tube assembly used in the experiment. The 19995 elements used in the simulation was validated via a convergence study that confirmed the strain results did not depend on the mesh. The driver tube was not modeled separately, as we are most concerned with the deflection in

the vicinity of the reflecting end. The applied pressure loading is given in Section 3 and corresponds to a stoichiometric ethylene–oxygen detonation of initial pressure 0.5 bar, 2 bar, or 3 bar. The two material models discussed above were used: mild steel using Cowper-Symonds rate-hardening and stainless steel with temperature independent Johnson-Cook material parameters. The boundary conditions used were a fixed boundary on the tube end where the detonation reflected (the right side of Fig. 17) and, on the opposite end, a boundary that was only confined in the radial direction to match the experimental conditions.

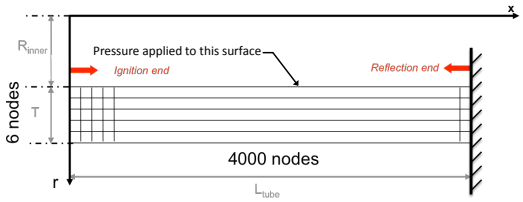

Figure 17: Mesh used for finite element computations in LS-DYNA. The detonation propagates from left to right, with the right boundary fixed and the left boundary confined in the radial direction alone.

6.1. 1010 Mild Steel Computations

Figure 18 contains the residual plastic strains calculated using the piecewise linear hardening model with Cowper-Symonds rate-hardening. The key thing to note in the comparisons shown in Fig. 18 is that the the two computations were performed using the same material model. Only the loading conditions were changed. Examining Fig. 18 (a) we see the strain response to five successive detonations of initial pressure 2 bar. The finite element simulation of the first experiment is quantitatively close to the experimental values in both strain amplitude and ripple wavelength. Although the errors grow in later experiments due to accumulation of error, the results are qualitatively correct. Similarly, the 3 bar initial pressure detonation comparison shown in Fig. 18 reveals that the first experiment is well predicted by the computation and later experiments remain qualitatively correct. This illustrates that properly incorporating the physics of gaseous detonations with appropriate material models allows for accurate prediction of material deformation.

Examining the locations where the computational model diverges from the experimental data allows us to understand the deficiencies of the present approach. The greatest disparity in peak strains between the model and the experiment occurs in the 2 bar case, where the maximum difference is 15% of the experimentally measured

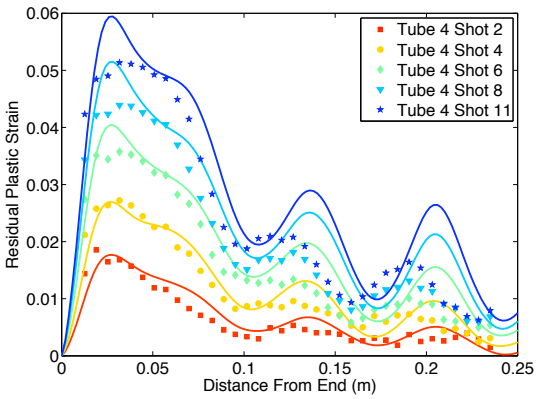

(a)

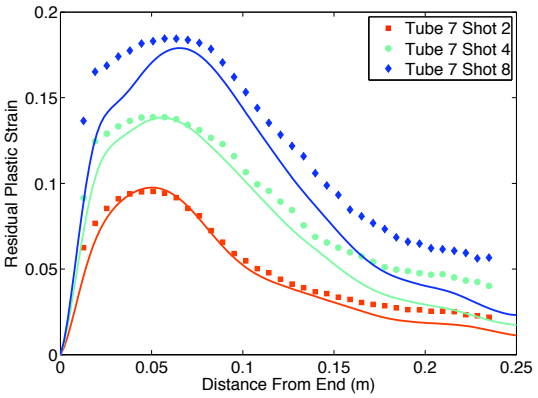

(b)

Figure 18: Comparisons of measured and calculated residual plastic hoop strains in mild steel for (a) five successive 2 bar initial pressure detonations in tube 4 and (b) three successive 3 bar initial pressure detonations in tube 7 using Cowper-Symonds rate-hardening. Experimental measurements are plotted as points and computed results are plotted as lines.

value. The underlying cause of these discrepancies is discussed with the stainless steel computational results in Section 6.2. The greatest deviation of peak strains in the 3 bar case occurs in the third experiment, where it is 3%. The error at this condition is substantially in excess of that found in the first two loading cycles of either tube. We speculate that this is due to the fact that this strain level is beyond the conditions for which we have measured and fit the material response. The model appears to be too hard for locations away from the peak strain in the 3 bar case; this may be the result of too early or steep a transition in tangent modulus.

6.2. 304L Stainless Steel Computations

LS-DYNA simulations using identical meshes and detonation loading conditions as the mild steel results

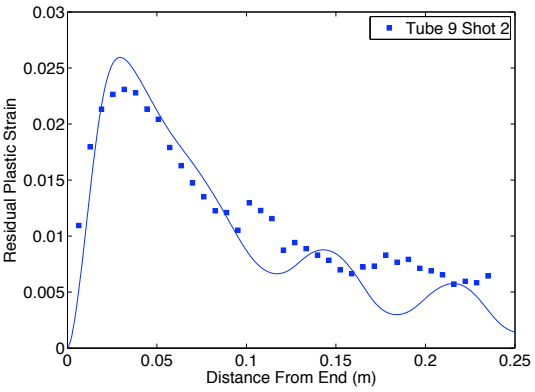

(a)

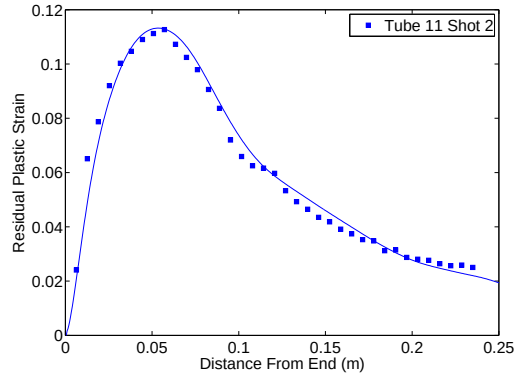

(b)

Figure 19: Comparisons of measured and LS-DYNA computed residual plastic hoop strains in stainless steel for a detonation of initial pressure (a) 2 bar and (b) 3 bar. LS-DYNA computations performed with the stainless steel Johnson-Cook material model. Experimental measurements are plotted as points and computed results are plotted as lines.

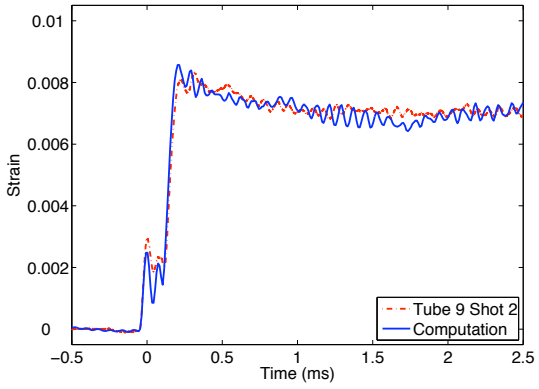

(a)

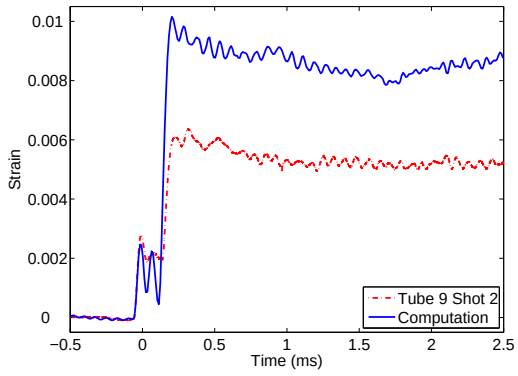

(b)

Figure 20: Comparisons of measured and LS-DYNA computed hoop strain-time traces for the first 2 bar detonation in stainless steel tube 9 at (a) 121 mm and (b) 146 mm away from the reflecting end. LS-DYNA computations performed with the stainless steel Johnson Cook material model.

discussed above were also performed using Johnson-Cook material parameters corresponding to 304L stainless steel as given in Table 5. Comparisons of the computational results with the first post-detonation outer diameter data for the 2 bar and 3 bar initial pressure experiments are shown in Fig. 19. In general, Fig. 19 (a) portrays good agreement between the modeled and measured residual plastic strain for the detonation of initial pressure 2 bar. The two areas of greatest error are in over-predicting the peak strain by 11% and with a misalignment between the locations of the local maxima of the ripple pattern. The cause of this misalignment in both these results and the above mild steel results is due to the sensitivity of residual plastic strain with the phase of the elastic oscillation as demonstrated with the above single degree of freedom results. This is portrayed in Fig. 20 where strain–time plots are given for both computations and measurements. In Fig. 20 (a), 121 mm away from the end wall, the two traces show very good agreement with one another, both in arrival time of the reflected wave and in the resulting strain. In Fig. 20 (b), however, 146 mm away from the end wall, the reflected shock in the model arrives nearly half of a natural period before the experimental case, resulting in a completely different excitation of the cross-sectional vibration. Thus we conclude that the initial oscillation is well-predicted by the finite element model with significant errors only originating after the arrival of the reflected shock due to misalignment in the phase of oscillation.

The agreement between computation and measurement is excellent for the detonation of initial pressure 3 bar as portrayed in Fig. 19 (b). Errors in the peak strain are only 0.44% and the maximum error is 4% and occurs at the location farthest from the reflecting end. This agreement is achieved by properly modeling both

the detonation pressure loading and the material properties. The reduction in error in the 3 bar case over the 2 bar case is due to the reduced effect that the elastic oscillation has on the residual plastic strain.

Figure 21 contains a comparison plot of the time histories of the strain gauges and the corresponding node locations in the finite element model. We observe that the deformation as a function of time is well predicted. The strains caused by the incident detonation are better predicted than those for the reflected shock wave which suffer from the interference effects discussed above; the computation shows discrepancies with experiment after the arrival of the reflected wave, illustrating the incredibly sensitive nature of the elastic calculations to minor differences in the reflected shock pressures and arrival times. Apart from the oscillation phase difference, we note that the the finite element model predicts a faster rise than that of the experimental result for the 2 bar initial pressure detonation. This is primarily due to the deficiencies of the pressure model, discussed in Section 3.

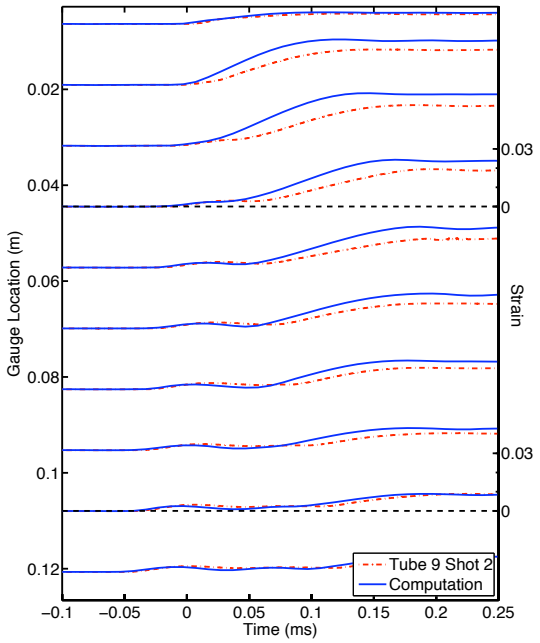

Figure 21: Hoop strain history comparison for the first 2 bar detonation in stainless steel tube 9. The experimental data are in red, and the results from the LS-DYNA finite element model are in blue.

7. Conclusions

Through careful consideration of both the experimental and computational details, we were able to achieve quantitatively accurate comparisons of strain data for steel tubes subjected to internal detonation loading. The single degree of freedom model explains the unique rippling pattern that was observed in the experiments and illustrates the counter-intuitive nature of the interaction between elastic and plastic effects in structures with repeated applied loadings. This model revealed that the ripple pattern was caused by the interference between the elastic oscillation induced by the incident detonation with the pressure loading created by the reflected shock wave and allowed the construction of an analytical solution predicting the ripple wavelength. The interference effect implies that small miscomputations of the phase of the elastic oscillation when the reflected wave arrives results in large deviations of final strain. And thus the comparisons of finite element computations with experiment are better when we consider the tube wall as a whole instead of strain–time histories at particular points.

This work also reinforces the necessity of properly accounting for strain-rate hardening when modeling impulsively applied loads characteristic of explosion testing. Accurate comparisons for the mild steel were only possible after testing the mild steel at the National Engineering School of Metz. However once an accurate material model is employed, this research demonstrates that the material deformation due to internal gaseous detonation may be quantitatively computed in both mild and stainless steel tubes for elastic motion and plastic deformations up to 10% using an accurate pressure model and material properties that properly account for plasticity and strain-rate effects. Careful control of the boundary conditions in the experiment described above combined with the accurate material models used in finite element modeling enables us for the first time to make quantitative predictions of residual plastic deformation for internal explosion loading of pipes.

Acknowledgements

This research is sponsored by the Department of Homeland Security through the University of Rhode Island, Center of Excellence for Explosives Detection. J. Damazo was supported by an NDSEG Fellowship.

References

Beltman, W., Shepherd, J., 2002. Linear elastic response of tubes to internal detonation loading. Journal of Sound and Vibration 252 (4), 617–655.

Browne, S., Zeigler, J., Shepherd, J., February 2008. Numerical solution methods for shock and detonation jump conditions. Tech. Rep. FM2006-006, Graduate Aeronautical Laboratories California Institute of Technology.

Cowper, G. R., Symonds, P. S., September 1957. Strain hardening and strain rate effects in the impact loading of cantilever beams. Technical Report 28, Brown University, Division of Applied Mechanics, Providence, RI.

Damazo, J., Chow-Yee, K., Karnesky, J., Shepherd, J. E., July 24–29 2011. Deformation of coated stainless steel tubes from reflected detonation. In: 23^{rd} Institute for Dynamics of Explosions and Reactive Systems. Irvine, CA, USA.

Deiterding, R., September 2003. Parallel adaptive simulation of multidimensional detonation structures. Ph.D. thesis, Brandenburgische Technische Universitat, Cottbus, Germany.

Deiterding, R., Cirak, F., Mauch, S., Meiron, D., 2006. Virtual test facility for simulating detonation-induced fracture of thin flexible shells. In: et al., N. A. (Ed.), Proc. Int. Conf. on Comp. Science, May 28-31, 2006, University of Reading. No. 3992 in Lecture Notes in Computer Science. Springer, Berlin, pp. 122–130.

Fickett, W., Davis, W. C., 1979. Detonation. University of California Press, Berkerely, CA.

Johnson, G. R., Cook, W. H., April 1983. A constitutive model and data for metals subjected to large strains, high strain rates and high temperatures. In: Seventh International Symposium on Ballistics. Vol. 7. the Hague Netherlands, pp. 541–547.

Karnesky, J., 2010. Detonation induced strain in tubes. Ph.D. thesis, California Institute of Technology.

Lee, J. H. S., 2008. The Detonation Phenomenon. Cambridge University Press, English translation of original Russian.

Lee, S., Barthelat, F., Hutchinson, J. W., Espinosa, H. D., 2006. Dynamic failure of metallic pyramidal truss core materials – experiments and modeling. International Journal of Plasticity 22, 2118–2145.

LS-Dyna, 2005. LS–DYNA User's Manual, version 971. Livermore Software Technology Corporation, Livermore, CA.

Radulescu, M. I., Hanson, R. K., Mar-Apr 2005. Effect of heat loss on pulse-detonation-engine flow fields and performance. Journal Of Propulsion And Power 21 (2), 274–285.

Rusinek, A., Klepaczko, J. R., 2000. A numerical study on the wave propagation in tensile and perforation test. J. Phys. IV France 10, 653–658.

Sauvelet, C., Rusinek, A., Shepherd, J. E., Liang, Z., Karnesky, J., 2007. Elastic and plastic deformation waves in tubes with internal gas explosion. In: ASME Applied Mechanics and Materials Conference. ASME, mCMAT2007-30024, presented June 3-7 2007 University of Texas at Austin.

Shepherd, J., Teodorcyzk, A., Knystautas, R., Lee, J., 1991. Shock waves produced by reflected detonations. Progress in Astronautics and Aeronautics 134, 244–264.

Shepherd, J. E., June 2009. Structural response of piping to internal gas detonation. Journal of Pressure Vessel Technology 131 (3), 87–115.

SolidWorks, 2007. SolidWorks Education Edition version 2007SP3.1. Dassault Systémes SolidWorks Corp., Concord, MA.

Taylor, G. I., 1950. The dynamics of the combustion products behind plane and spherical detonation fronts in explosives. Proc. Roy. Soc. A200, 235–247.

Wintenberger, E., Austin, J. M., Cooper, M., Jackson, S., Shepherd, J. E., 2004. Reply to 'comment on analytical model for the impulse of single-cycle pulse detonation tube'. Journal of Propulsion and Power 20 (5), 957–959.

Zaera, R., Rodríguez-Martínez, J. A., Casado, A., Fernández-Sáez, J., Rusinek, A., Pesci, R., 2012. A constitutive model for analyzing martensite formation in austenitic steels deforming at high strain rates. International Journal of Plasticity 29, 77–101.

Zel'dovich, Y. B., 1940. On the theory of the propagation of detonations in gaseous systems. JETP 10, 542–568, available in translation as NACA TM 1261 (1950).

Zel'dovich, Y. B., Kompaneets, A. S., 1960. Theory of Detonation. Academic Press, NY, english translation of original Russian.

Ziegler, J., 2010. private communication.